Check for updates

OPTICS

Optical corner detection with azimuthal Hilbert transform metasurfaces

Chen Chen[1,2]†, Junyi Wang[1]†, Rong Lin[2], Jiacheng Sun[1], Wange Song[1], Shining Zhu[1], Tao Li[1]*, Din Ping Tsai[2,3,4]*

Copyright © 2026 The Authors, some rights reserved; exclusive licensee American Association for the Advancement of Science. No claim to original U.S. Government Works. Distributed under a Creative Commons Attribution NonCommercial License 4.0 (CC BY-NC).

Many animals efficiently interpret their environment by detecting geometric features like corners, highlighting the power of feature extraction for reducing visual complexity; similarly, with the surge in visual data, nature-inspired optical corner detection offers a promising yet still elusive solution for energy-efficient information processing and compression. Here, we propose a universal strategy for optical corner imaging with azimuthal Hilbert transformation metasurfaces. Multiple objects, regardless of their amplitude, phase, or angular characteristics, can be detected simultaneously with a single metasurface, featuring broadband and full–field-of-view properties. Trade-offs between spatial and angular resolution are assessed, offering practical guidance for implementation. We further demonstrate motion tracking as a proof-of-concept application leveraging the data-compressed corner imaging framework. This work paves the way for next-generation optical information processing technologies.

INTRODUCTION

In nature, many animals' visual systems are particularly attuned to geometric features such as corners. For example, bees use their compound eyes to detect sharp angles or indentations on flowers and show a preference for complex, angular shapes (*1*, *2*). Woodpeckers often peck at the intersections of bark cracks or insect holes (*3*), which are corner-like cues that suggest hidden insects. Predators such as cats and cheetahs focus on abrupt changes along the prey's outline, like joints or the tail base, to anticipate movement direction (*4*, *5*). These examples illustrate that, while animal vision typically integrates a range of cues, certain species demonstrate heightened sensitivity to corners or localized high-contrast features. This insight from nature highlights the efficiency of feature extraction, which is essentially a process of subtraction, over the pursuit of ever-richer, multidimensional information. Especially in today's era of information overload, corner detection offers a powerful and cost-effective way to reduce visual complexity, although it continues to pose challenges.

Recent advances in metasurfaces (*6*–*8*), notably their ability to precisely manipulate wavefronts at the subwavelength scale, have enabled the development of highly efficient and compact optical processing devices (*9*–*17*). In particular, metasurfaces have been engineered to perform optical edge detection (*10*, *11*, *18*–*22*), a fundamental feature extraction operation intimately linked to differentiation. While edge detection effectively reduces dimensionality by compressing two-dimensional (2D) image information into contour features, the exponential growth in demand for information compression efficiency in the era of big data has made further reduction from 2D features to 1D key points an inevitable trend. As a representative 1D feature extraction method, corner detection mathematically corresponds to identifying curvature extrema in images, supporting critical computer vision applications such as image registration, object recognition, and 3D reconstruction (*23*–*27*). However, despite its importance, practical optical solutions for corner detection remain elusive.

In this work, a general optical corner detection method is proposed on the basis of metasurfaces with azimuthal Hilbert transforming capability. Leveraging the unique manipulation of frequency components, we first demonstrated direct imaging detection of corners with different angular characteristics, respectively. Experimental results manifest straightforward corner-highlight imaging with broadband and full–field-of-view properties in the visible region. The multifunctionality of simultaneously detecting different kinds of corners with a single metasurface was further demonstrated, together with the analysis of the trade-off between spatial resolution and angular resolution. Last, object motion tracking was successfully performed on the basis of the sequentially captured corner-detection images, showcasing the full potential of next-generation, high-speed optical information processing systems.

RESULTS

Principle of the optical corner detection with metasurface

To realize optical corner detection, we consider modulating its angular spectrum with a certain spatial interference effect to extract the desired corner information. For an input optical image $E_{in}(x, y)$, its angular spectrum $A(k_x, k_y)$ can be expressed as

$$A(k_x, k_y) = \mathcal{F}\left[E_{in}(x, y)\right] = \iint E_{in}(x, y)\exp\left(-ik_x x - ik_y y\right)dxdy \quad (1)$$

where i is the imaginary unit, $\mathcal{F}$ indicates the Fourier transform, and k_x, k_y are 2D Fourier domain variables along the x and y directions. If an optical transfer function $t(k_x, k_y)$ is exerted on the frequency components, then the output image $E_{out}(x,y)$ becomes

$$E_{out}(x, y) = \iint t(k_x, k_y)A(k_x, k_y)\exp\left(ik_x x + ik_y y\right)dk_x dk_y \quad (2)$$

[1]Nanjing University, National Laboratory of Solid State Microstructures, Key Laboratory of Intelligent Optical Sensing and Manipulations, Jiangsu Key Laboratory of Artificial Functional Materials, Collaborative innovation center of advanced microstructures, College of Engineering and Applied Sciences, Nanjing 210093, China. [2]Department of Electrical Engineering, City University of Hong Kong, Kowloon, Hong Kong, SAR 999077, China. [3]State Key Laboratory of Terahertz and Millimeter Waves, City University of Hong Kong, Kowloon, Hong Kong, SAR 999077, China. [4]Department of Physics, City University of Hong Kong, Kowloon, Hong Kong, SAR 999077, China.
*Corresponding author. Email: taoli@nju.edu.cn (T.L.); dptsai@cityu.edu.hk (D.P.T.)
†These authors contributed equally to this work.

Downloaded from https://www.science.org on May 06, 2026

which could also be expressed in another form as

$$E_{out}(x,y) = E_{in}(x,y) * T(x,y) \quad (3)$$

where $T(x,y) = \mathcal{F}^{-1}[t(k_x,k_y)]$, and $\mathcal{F}^{-1}$ indicates the inverse Fourier transform.

Here, inspired by the algorithm in digital signal processing (*28*), we propose the concept of azimuthal Hilbert transform (termed as AHT) to serve as an optical transfer function $t(k_x, k_y)$. For a straightforward demonstration, a common 4*f* imaging system is used to perform the Fourier transform. As shown in Fig. 1A, the object is placed at the front focal plane of the first optical lens, and the AHT metasurface is positioned at the back focal plane to manipulate the spatial spectrum features. The second lens successively performs the inverse Fourier transform of the signal and displays the corner information in the spatial space.

The azimuth Hilbert transform is exemplarily displayed in Fig. 1B. It features a step-type phase distribution with varying azimuth angles and can be expressed as

$$t(k_x,k_y) = e^{i\varphi(k_x,k_y)} = \begin{cases} 1, \textit{if floor}\left[\arctan\left(\frac{k_y}{k_x}\right)/\theta\right] \text{ is even number} \\ -1, \textit{if floor}\left[\arctan\left(\frac{k_y}{k_x}\right)/\theta\right] \text{ is odd number} \end{cases} \quad (4)$$

where *floor* (a/b) is the quotient when a is divided by b, θ is the equally spaced central angle in the Fourier plane, and would directly influence the detectable corner angle, which will be discussed in detail in the following part.

To achieve robust and broadband phase modulation, the Pancharatnam-Berry (PB) phase (*29*) is used. The distribution of meta-atoms with varying orientation angles (β), which enables a phase control of $\varphi = \pm 2\beta$, is schematically illustrated above the phase profile in Fig. 1B. In the neighboring segment, the meta-atoms all share an orientation angle difference of 90°, corresponding to a π phase shift.

For a proof of concept, silicon nitride (SiN_x) with low loss in the visible and complementary metal-oxide semiconductor compatibility is chosen as the material for the meta-atoms. As illustrated in the bottom left of Fig. 1A, the unit cell with a substrate of silicon dioxide (SiO_2) is arranged in a hexagonal lattice with a lattice constant of 360 nm to satisfy the subwavelength requirement in the visible wavelength range of 450 to 680 nm. On the basis of the finite-difference time-domain simulation, the parameters of the nanorod are optimized to a size of 120 nm by 280 nm by 1200 nm ($w \times l \times h$) with a high average transmittance up to 97% and average efficiency up to 81% (see fig. S1 for details). Here, the efficiency is defined as the transmitted energy of cross-circular polarization light divided by that of the incident circular polarization light.

In experiments, we first designed the AHT metasurfaces with different values of θ, including 60°, 30°, and 10°. With the standard electron-beam lithography and dry etching process (see Materials and Methods and fig. S2), these metasurfaces have been successfully fabricated and characterized. Figure 1 (C to E) shows the sample information for the metasurface with θ = 30°, with others displayed in fig. S3. The diameter of the metasurface is 1 mm, and the optical micrograph reveals discernible zoning patterns in the sample due to the abrupt change of meta-atom orientations. Figure 1D displays top-view and tilted-view scanning electron microscopy (SEM) images, exhibiting

Downloaded from https://www.science.org on May 06, 2026

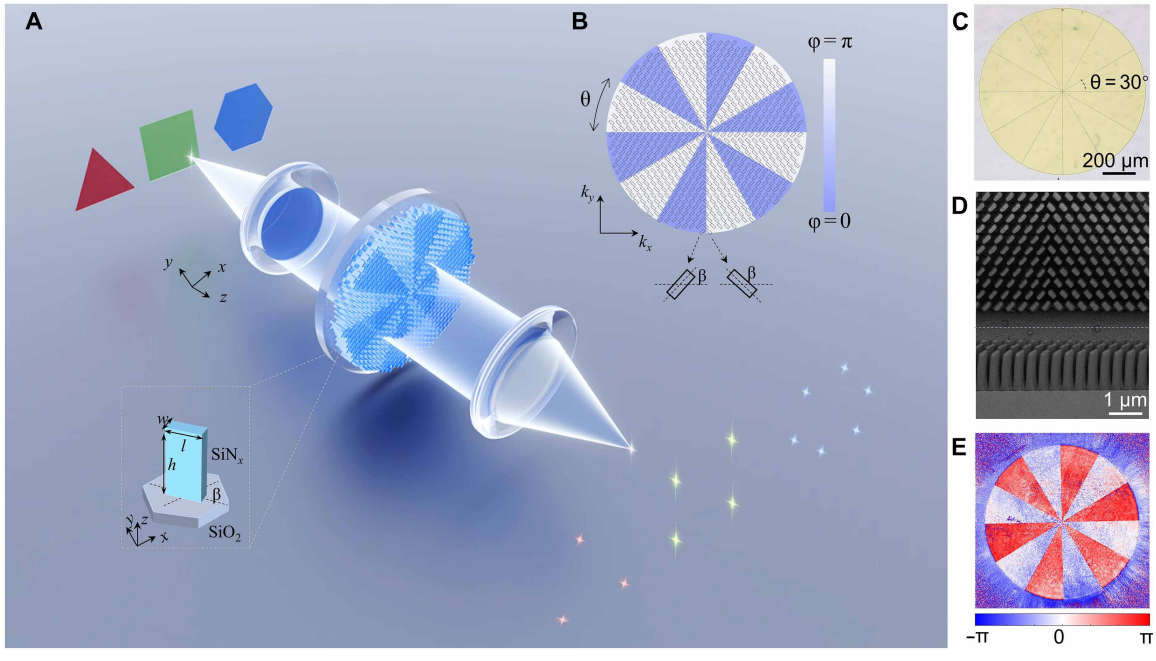

Fig. 1. Schematic of the optical corner detection and the metasurface sample information. (**A**) Setup for optical corner detection imaging, which is composed of a 4*f* imaging system, and the metasurface is placed in the middle of the Fourier plane. The enlarged part shows the used meta-atom for PB phase modulation. (**B**) Schematic diagram of the phase profile of the azimuthal Hilbert transform metasurface, accompanied by its corresponding meta-atom arrangement. (**C**) Optical microscopy image of the fabricated AHT metasurfaces designed with θ = 30°. (**D**) SEM images from top view and oblique view. (**E**) Measured phase distribution of the AHT metasurface at λ = 532 nm.

well-defined morphology in all three dimensions. We further used an interferometric imaging system to measure the phase distribution. Figure 1E presents the results at λ = 532 nm obtained under illumination with left circularly polarized (LCP) light and subsequent right circularly polarized (RCP) light analysis, exhibiting excellent agreement with the designed azimuthal π-phase staircase profile. Such phase modulation is maintained when exchanging the polarization states (LCP detection with RCP illumination). Leveraging the broadband nature of the PB phase, wavelength-independent phase response is observed across the visible spectrum, as corroborated by fig. S4, which shows consistent phase results at other wavelengths.

Experimental demonstration of the basic detection properties

After characterizing the fabricated metasurfaces, we demonstrated the basic corner detection capability. A triple-wavelength laser imaging system was built to measure its broadband characteristics (details see Materials and Methods and fig. S5). Different polygonal patterns were fabricated through electron-beam lithography to act as imaging objects located at the first Fourier plane. The metasurface was placed at the intermediate Fourier plane to conduct the AHT operations, and a color camera (FLIR, BFS-U3-200S6C-C, pixel size: 2.4 μm by 2.4 μm) was placed at the back focal plane of the Fourier transform system for the image acquisition. Figure 2 (A to C) illustrates the imaging results under red light with λ = 638 nm. The first row displays the bright-field images without metasurfaces. When adding the AHT metasurface with θ = 60° into the setup, the light field around the corners with angles of 60° or 120° would experience destructive interference, leaving the corners highlighted. As shown in the bottom row of Fig. 2A, the corners of a regular triangle and a regular hexagon were manifested distinctly. Similarly, the AHT metasurface with θ = 30° is also perfect for corners with angles of 30° or 150°. Figure 2B shows the detection results for a regular dodecagon (also termed as 12-gon), with evenly distributed light points in accordance with the corners. Figure 2C further displays the results of the metasurface with θ = 10°. In the bright-field image of a regular 36-gon, the corners exhibit negligible contrast to the naked eye. However, upon incorporating the metasurface, the corner positions emerged clearly. The specific profiles of the corner points are decided by the convolution process and would appear differently in different situations.

The detection capabilities remain consistent when switching to other visible illumination wavelengths due to the wavelength-independent phase modulation and destructive interference effect, as part of the broadband results at λ = 450 and 532 nm illustrated in Fig. 2D (details

Downloaded from https://www.science.org on May 06, 2026

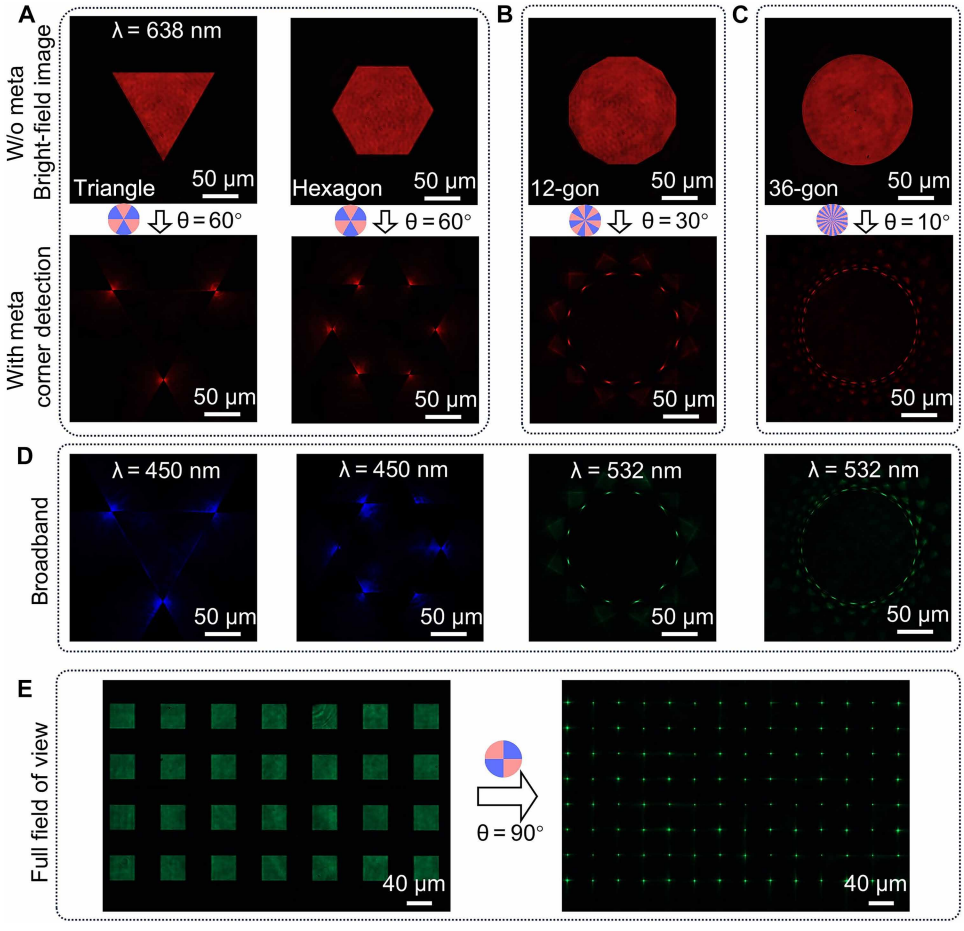

Fig. 2. Characterization of the basic corner detection properties. Imaging results with the metasurface of (**A**) θ = 60°, (**B**) θ = 30°, and (**C**) θ = 10°. The top panel is the corresponding bright-field images without metasurfaces. (**D**) Broadband imaging results for corner detection. (**E**) Full–field-of-view imaging results using the metasurface with θ = 90°, and the left panel is the related bright-field image.

in fig. S6). In addition, the optical modulation on the Fourier plane can apply the same analog computation process to the entire field of view when the imaging optical elements are near aberration free. To demonstrate the full–field-of-view imaging property in an orderly way, a periodically arranged square pattern (Fig. 2E, left) was chosen as the imaging object, where the AHT metasurface becomes quadrantally divided with $\theta = 90°$. Here, the phase profile is simplified to that of second-order partial derivatives. The details of the sample, including the optical micrograph, the SEM image, and measured phase profiles, are shown in fig. S7. Figure 2E (right) displays the corner detection image, with every bright point coinciding precisely with its corresponding square corner across the whole sensor area. While the presented results mainly focused on micrometer-scale objects, it would also be effective for larger, centimeter-scale objects; see fig. S8, indicating potential applications at the macroscopic scale as well.

Trade-off between spatial resolution and angular resolution

In the above part, we used a specific AHT metasurface to detect corners with related angles. When the metasurface has a steeper azimuthal π phase shift, corresponding to a smaller value of θ, it can detect more subtle changes in angle, i.e., features with higher angular resolution (evidenced by the results in Fig. 2C). Yet, logically, the AHT metasurface designed with a small θ could also be used to detect larger corner angles. Taking the square object as an example, the obvious solution for corner detection is an AHT metasurface with $\theta_0 = 90°$, as previously demonstrated in Fig. 2E. While for an AHT metasurface with θ, where $\theta \in \{\theta_0/n \,\&\, 2\pi/m \mid n, m \in \mathbb{N}^+\}$, it can also detect the related corners. Here, θ can be 45°, 30°, 22.5°, 18°, 15°, 11.25°, 10°, 9°, 7.5°, 6°, 5.625°, 5°, 4.5°, etc. As can be seen from the first column in Fig. 3, the AHT metasurfaces with $\theta = 30°$ and 10° exemplarily demonstrated the extended detection capability.

It is therefore of interest to determine the smallest detectable value of θ, that is, to explore the limit of angular resolution. Although reaching these limits experimentally can be challenging, we find that improving angular resolution may come at the expense of spatial resolution, as demonstrated below. The square patterns were fabricated with different side lengths (d) from 120 to 5 μm to obtain the systematic imaging results. Figure 3A shows the bright-field images without metasurfaces, and Fig. 3 (B to D) displays the corner detection results acquired through metasurfaces with $\theta = 10°$, 30°, and 90°, respectively. The cases with distinct corners are framed by red boxes in Fig. 3 (B to D), showing that the side length with discernible corner detection reduces from 20 to 5 μm when the θ increases from 10° to 90°. A similar phenomenon also occurs when the object contrast is inverted from positive to

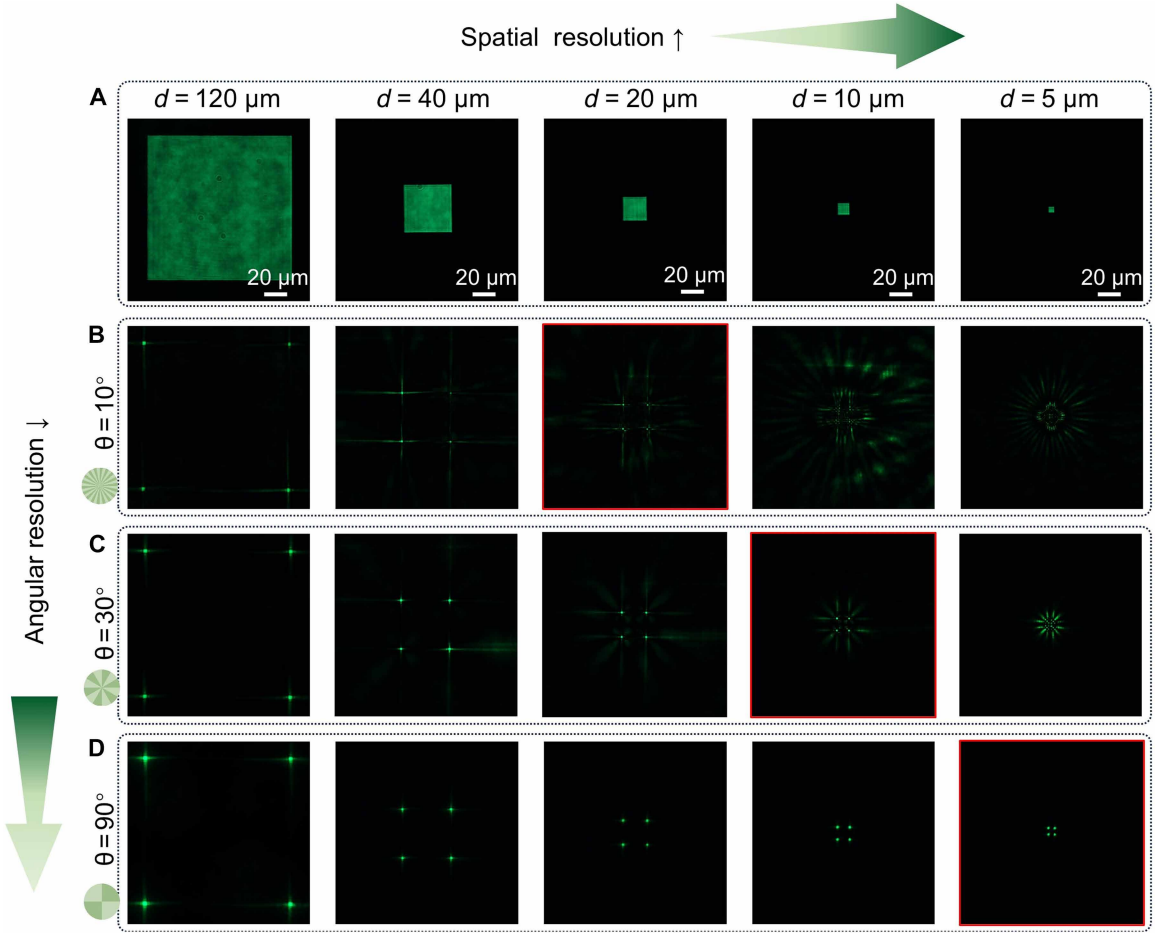

Fig. 3. Trade-off between angular resolution and spatial resolution. (**A**) Bright-field images of the square patterns with different dimensions. Corner detection results acquired through AHT metasurfaces with (**B**) $\theta = 10°$, (**C**) 30°, and (**D**) 90°. Red boxes indicate the corresponding pattern dimensions with discernible corners. Here, the displayed images were acquired with different exposure times to optimize the visibility of each object size.

Downloaded from https://www.science.org on May 06, 2026

negative (see fig. S9 for details). Here, the corner discernibility is determined by evaluating whether the highlighted bright spot is the intensity peak in a small neighborhood around the corner and matches the corner position, which is termed as local intensity peak criterion (see text S1 and figs. S10 to S12 for more details). This trade-off between angular resolution and spatial resolution demonstrated here arises because the coherent point spread function (PSF) of the system with higher angular resolution becomes larger, which can induce a more distinct tailing phenomenon due to interference when the imaging object becomes smaller. The spatial resolution analyzed in Fig. 3 mainly refers to the object size with the effective corner highlighted effect. When the object size satisfies the required criteria (approximately the size of the PSF), the distinguishable distance between two neighboring corners is about the diffraction limit (λ/NA, where NA is the abbreviation of numerical aperture).

Figure 4 provides a detailed illustration of the criteria, primarily derived from simulations to mitigate the effects of experimental errors. In the simulation, the system's NA (~0.34) and working wavelength (532 nm) were set to be identical to those in the experiment, which gives a diffraction-limited resolution of ~1.6 μm. The PSF sizes (defined as the diameter of the first ring L) of the systems with different angular resolution are shown in the left column of Fig. 4A, approximately 2, 5, and 11 μm for θ = 90°, 30°, and 10°, respectively. The corner detection images of square objects with varying sizes d are displayed alongside the corresponding PSFs. The images of the objects are superimposed on the corner detection images for better illustration. In all three cases, noticeable corner detection effects are observed when the object size approaches or exceeds the system's PSF (highlighted by the red box), aligning well with the experimental phenomenon. Here, the corner discernibility is determined following the local intensity peak criterion and also complemented by whether the image rotates. Furthermore, when the object size reaches the detectable criteria (e.g., larger than 11 μm at θ = 10°), two adjacent corners can only be distinguished when the separation distance exceeds λ/NA, indicating the diffraction-limited resolution of the corner detection system (Fig. 4B). An experimental and simulated corner detection image of a resolution chart at θ = 90° is also discussed in fig. S13 with detailed simulation procedures shown in text S2, further

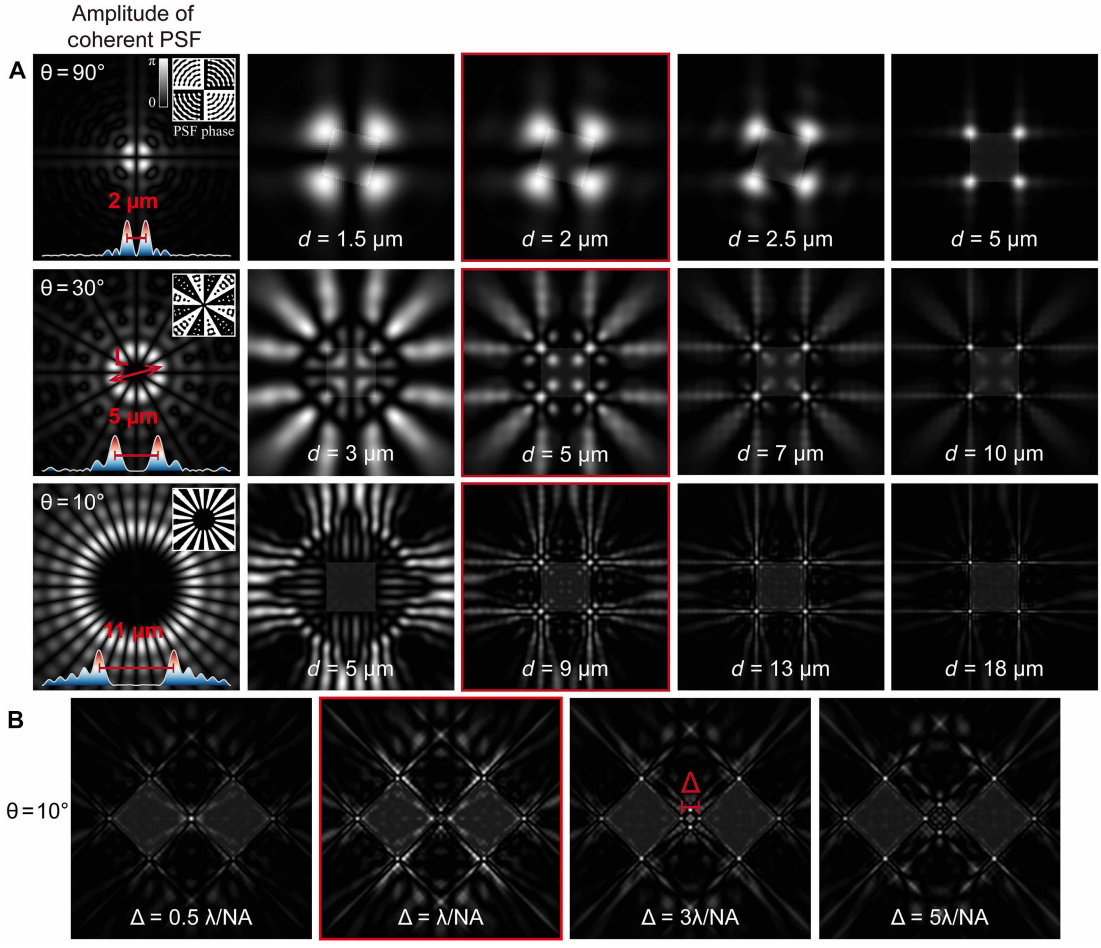

Fig. 4. Criteria for diffraction-limited corner detection imaging. (**A**) Object size criteria. The first column shows the amplitude profiles of coherent PSF, and the inset corresponds to the phase distribution. The sizes of the PSFs are approximated with the diameter of the first ring (L). Other columns display the related corner detection images with varying object sizes. In the case of θ = 90°, the squares for the first three object sizes are rotated by 20° to enable a clearer recognition of the corner detection effect. The respective object size (d) with discernible corner highlighting effect is framed with a red box. (**B**) Separation distance criteria. The side length of the simulated square is set as 16 μm, which satisfies the object size criterion for the system with θ = 10°. The distances (Δ) between the two adjacent corners vary from 0.5 to 5λ/NA. The red box marks the diffraction-limited case.

Downloaded from https://www.science.org on May 06, 2026

illustrating the diffraction-limited spatial resolution of the system. Therefore, it is advisable to consider these criteria (i.e., object size and separation distance) and select an appropriate angular resolution in different cases rather than applying a consistent small θ in all detection scenarios.

Multifunctional detection and motion tracking application

In the previous section, we mentioned that the AHT metasurface with a smaller θ could be used for the detection of corners with larger angles. This also indicates that such an AHT metasurface could be used for the simultaneous detection of different-angle–featured corners. A nested pattern incorporating triangle, square, and hexagon was designed and fabricated through electron beam lithography, with the bright-field image shown in Fig. 5A (left). By inserting the AHT metasurface with θ = 30°, the corner positions distinguish themselves through unique features. For each corner of the hexagon, it appears as two crossed lines along the initial direction, with the intersection point being a dark dot (see Fig. 5A, middle). Concerning the negative square pattern, the corner position emerges as a bright dot with a negligible cross-shaped tail, consistent with the results shown in Fig. 3C. It also indicates the effectiveness of corner detection for the other negative patterns. When it comes to the triangle situation, the corner characteristic is similar to that of the hexagon. The detected corner signal is weaker for the smaller object, consistent with the reduced input energy (see text S3 and fig. S14 for details). Therefore, we magnified this section and enhanced its brightness and contrast for improved clarity, as illustrated in Fig. 5A (right). The corner position also appears as a dark dot, while the cross lines in the upper corners exhibit nonuniform intensity distributions compared to the one in the lower region, resulting from the convolution process characteristics. Specifically, the corner with angle of α emerges as a bright point if α/θ is an odd number, and it emerges as a dark point if α/θ is an even number (see text S4 for details and explanations). All these distinctive features enable the differentiation between various corner types.

In addition to the amplitude patterns, such an AHT metasurface also works for the phase objects. A SiN_x film was deposited on a quartz substrate, followed by electron beam lithography and etching processes (similar to the fabrication of metasurfaces) to fabricate the corresponding phase-modulating structures. Although the fabricated phase object had the same pattern as the amplitude object in phase, the features exhibit low contrast against the background in the bright-field image (Fig. 5B, left), resulting in minimal visual distinction. With the incorporation of AHT metasurface (θ = 30°), the corners manifest the same characteristics as the amplitude case (Fig. 5B, middle and right), demonstrating the scheme's effectiveness for phase objects. More results with other illumination wavelengths for the phase objects are shown in fig. S15, further exhibiting the broadband operational capability.

The AHT metasurface–enabled corner detection can achieve data compression with simultaneous feature enhancement, facilitating rapid analysis, interpretation, and measurement workflows. We further designed a motion tracking experiment to illustrate its advantages and potential applications. A square mask with a side length of 120 μm was chosen as the observation object and was randomly moved and rotated 18 times within the field of view, as schematically shown in Fig. 5C. With each movement, the camera captures the corner detection image in sequence at λ = 638 nm using an AHT-metasurface with θ = 10°. Such corner featured images are more convenient for positioning, and by analyzing the coordinates of the corners, the moving trajectory can be easily resolved. Figure 5D depicts the coordinated distribution of the mask (center of the four corners), where the blue line marks the

Downloaded from https://www.science.org on May 06, 2026

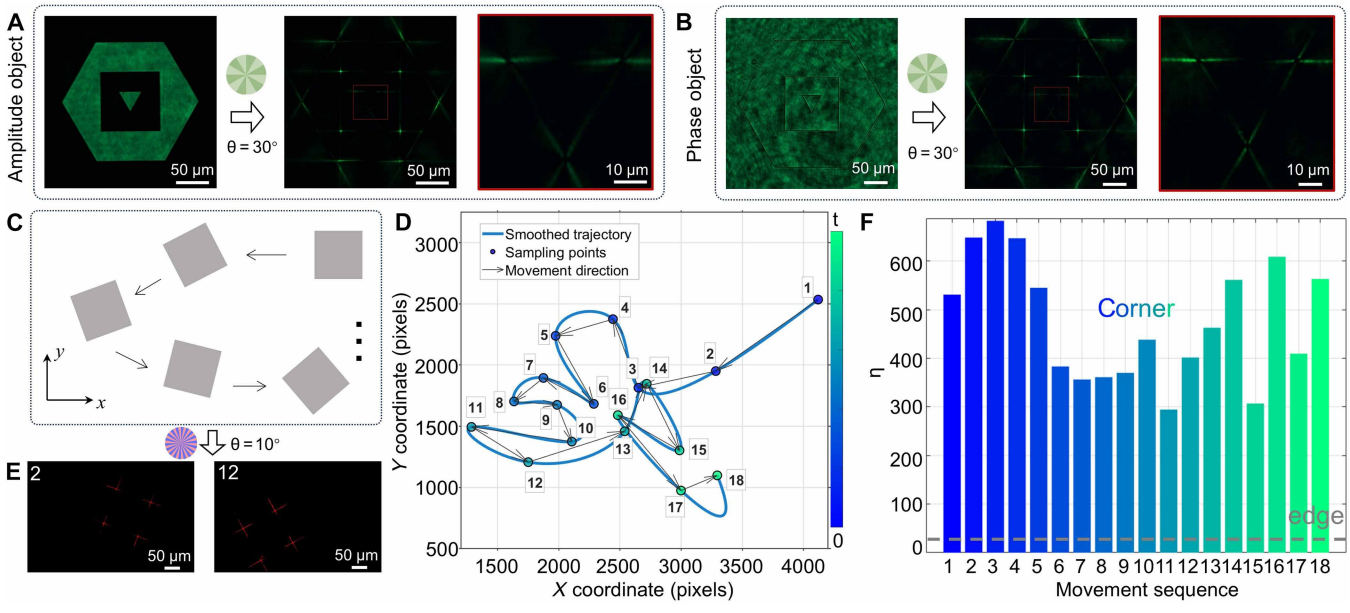

Fig. 5. Experimental results for multifunctionality and motion tracking application. Simultaneous detection of the corners with different angle features for (**A**) an amplitude object, and (**B**) a phase object. The left panel is the bright-field image, the middle panel is the detection result, and the right panel is the enlarged region in the middle panel. (**C**) Schematic of the random object movement and rotation. (**D**) Analyzed movement trajectory. (**E**) Selected corner detection image results, including the 2nd and the 12th images. (**F**) Data-compression ratio (η) distribution for corner detection images, and the bottom gray dashed line indicates the average ratio for edge detection images.

smoothed trajectory and the arrow denotes the movement direction. Movement iterations are numerically indexed, with chromatic mapping of the sampling points indicating the temporal evolution. The image results are selectively shown in Fig. 5E (the 2nd and the 12th images), and the complete data are listed in fig. S16 and displayed as a supplementary movie for detailed correspondence. The motion tracking application could also be extended to other objects with distinct corner features. To illustrate the data-compression capability, we defined a data-compression ratio (η) as the total effective pixels of original bright-field images (N_{ori}) divided by those of the corner detection images (N_{cor}). In this case, η is calculated and displayed in Fig. 5F with an average value of $\eta \approx 476$. For comparison, the gray dashed line at the bottom is the average η calculated for the traditional edge detection, valuing around 18 (details see figs. S17 to S19). The data-compression capability of the corner detection outperforms the edge detection by an order of magnitude, and such advantages would increase quadratically with the object size, highlighting its superiority in data compression for even larger objects. It is worth mentioning that the increased compression may come at the expense of losing certain image details, particularly those not captured by corner features; thus, the choice between corner- and edge-based schemes should ultimately be guided by the requirements of the target application: For tasks that primarily rely on salient structural landmarks or object localization, corner-based compression is highly advantageous, whereas applications demanding fine-grained texture, contour fidelity, or high-accuracy reconstruction may benefit more from edge-based or hybrid feature representations.

DISCUSSION

We propose a strategy of azimuthal Hilbert transform metasurface to realize optical corner detection imaging. It is a systematic demonstration of the identification of different types of corners. The proposed imaging scheme features broadband and full field-of-view capabilities. Using the single meta-phase modulation, it is possible to simultaneously detect multiple objects regardless of their amplitude, phase, or angular characteristics. The trade-off between the imaging spatial resolution and angular resolution was further analyzed experimentally, offering additional insights for design and practical applications. Considering the benefits of positioning and identification, a motion tracking experiment was ultimately conducted on the basis of the data-compressed corner detection imaging.

The metasurface design offers several key benefits over commercial phase plates, including subwavelength spatial resolution, the ability to engineer highly complex and spatially varying phase profiles, and the potential for on-chip integration. The realized corner-detection function is a higher-level vision primitive that requires the joint analysis of gradients along different directions. It offers substantially greater data compression capabilities than traditional edge detection, and the AHT metasurface can accomplish multiple differential operations in different directions simultaneously, distinguishing it from other differential techniques. In the contemporary era of information explosion, the demand for highly efficient feature extraction imaging is rapidly increasing across a wide range of fields, including biomedical imaging, augmented reality, machine vision, and autonomous vehicles. Although digital signal processing can offer great versatility, it faces challenges like substantial energy consumption and speed limitation due to the low response of electrons (*30*, *31*). In contrast, the strategy presented here is grounded in analog computing paradigms using photons, which may offer substantial advantages (*32*). By harnessing the intrinsic parallelism and ultralow power consumption of photons through wavefront manipulation, our methods could open up avenues for constructing next-generation, high-speed, energy-efficient image processing systems.

Our method was validated in the visible spectrum, while it can be extended to other wavelength regions, nourishing applications across diverse fields from the micro- to the macro-information processing. This represents a notable advancement in dimensionality reduction for optical imaging with data analysis. The presented approach provides a fundamental design paradigm for optical corner detection. Its versatility can be substantially enhanced through multiplexing strategies, which enable the extraction of multiple corner features and thereby increase the generality and applicability of our method (see text S5 and figs. S20 to S22). The corner detection can also be realized using a single metalens without a 4*f* configuration (see text S6 and fig. S23), representing an important step toward device-level implementation of our design. Future developments include the integration of the analog computation process into a singlet metasurface along with aberration correction, the resolution enhancement both in spatial and angular space, the design for incoherent environments, the optimization for other application scenarios, etc.

MATERIALS AND METHODS

Sample fabrication

The SiN_x layer was deposited on the dry-cleaned fused silica substrate using the plasma-enhanced chemical vapor deposition to a final thickness of 1000 nm. Then, 200 nm of polymethyl methacrylate A4 photoresist film is spin-coated onto the substrate and baked at 170°C for 5 min. A layer of water-soluble conductive polymer (AR-PC 5092) was spin-coated on the resist for the dissipation of E-beam charges. The device pattern was written on an electron beam resist using an E-beam writer (Elionix, ELS-F125). An electron beam evaporated chromium layer was used to reverse the generated pattern with a lift-off process and was then used as a hard mask for dry etching the SiN_x layer. After that, the devices were transferred into the OXFORD PP100 Plasma Etcher and etched with SF6 and CHF3 (the flow rates of these two types of gases are 6:60 standard cubic centimeter per minute). Last, the chromium layer was removed by a stripping solution (ceric ammonium nitrate).

Experimental characterization

Three laser sources (LDM10-450/520/638, Jcoptix) were used as the incident light and switched using two reflecting mirrors (BDM1-T1-A-SP, LBTEK). An objective lens [20×, numerical aperture (NA) 0.4, GCO-2132, Daheng Optics] was combined with a 15-μm pinhole to form a spatial filter. The spatial filter was inserted after the source to create a clean, divergent optical field, which was then collimated by an achromatic lens (OLD2440-T2M, Jcoptix) to illuminate the sample. An objective lens (NA0.6, 20×) and a tube lens (TTL200-A, Thorlabs) formed a customized microscope system. Two objective lenses with the same focal length of 50 mm (field number: 2.4, MVL-KF2524M-25MP, HIKROBOT) functioned as an optical Fourier transform system. The magnified image was transferred to the front focal plane of the Fourier transform system by the microscope. The metasurface was placed at the intermediate Fourier plane to conduct analog operations. A color camera (FLIR, BFS-U3-200S6C-C) was placed at the back focal plane of the Fourier transform system for the image acquisition.

Downloaded from https://www.science.org on May 06, 2026

Supplementary Materials

The PDF file includes:

Supplementary Text S1 to S6
Figs. S1 to S23
Legends for movies S1 and S2
References

Other Supplementary Material for this manuscript includes the following:

Movies S1 and S2

REFERENCES

1. M. Lehrer, M. V. Srinivasan, S. W. Zhang, G. A. Horridge, Motion cues provide the bee's visual world with a third dimension. *Nature* **332**, 356–357 (1988).
2. G. A. Horridge, What does an insect see? *J. Exp. Biol.* **212**, 3494–3501 (2009).
3. G. R. Martin, *The Sensory Ecology of Birds* (Oxford Univ. Press, 2017).
4. G. Johansson, Visual perception of biological motion and a model for its analysis. *Percept. Psychophys.* **14**, 201–211 (1973).
5. M. F. Land, D. E. Nilsson, *Animal Eyes* (Oxford Univ. Press, 2012).
6. T. Li, C. Chen, X. Xiao, J. Chen, S. Hu, S. Zhu, Revolutionary meta-imaging: From superlens to metalens. *Photon. Insights* **2**, 10.3788/PI.2023.R01 (2023).
7. A. I. Kuznetsov, M. L. Brongersma, J. Yao, M. K. Chen, U. Levy, D. P. Tsai, N. I. Zheludev, A. Faraon, A. Arbabi, N. Yu, D. Chanda, K. B. Crozier, A. V. Kildishev, H. Wang, J. K. W. Yang, J. G. Valentine, P. Genevet, J. A. Fan, O. D. Miller, A. Majumdar, J. E. Fröch, D. Brady, F. Heide, A. Veeraraghavan, N. Engheta, A. Alù, A. Polman, H. A. Atwater, P. Thureja, R. Paniagua-Dominguez, S. T. Ha, A. I. Barreda, J. A. Schuller, I. Staude, G. Grinblat, Y. Kivshar, S. Peana, S. F. Yelin, A. Senichev, V. M. Shalaev, S. Saha, A. Boltasseva, J. Rho, D. K. Oh, J. Kim, J. Park, R. Devlin, R. A. Pala, Roadmap for optical metasurfaces. *ACS Photonics* **11**, 816–865 (2024).
8. M. L. Brongersma, R. A. Pala, H. Altug, F. Capasso, W. T. Chen, A. Majumdar, H. A. Atwater, The second optical metasurface revolution: Moving from science to technology. *Nat. Rev. Electr. Eng.* **2**, 125–143 (2025).
9. Y. Zhou, H. Zheng, I. I. Kravchenko, J. Valentine, Flat optics for image differentiation. *Nat. Photonics* **14**, 316–323 (2020).
10. M. Cotrufo, A. Arora, S. Singh, A. Alù, Dispersion engineered metasurfaces for broadband, high-NA, high-efficiency, dual-polarization analog image processing. *Nat. Commun.* **14**, 7078 (2023).
11. X. Qiu, J. Zhang, Y. Fan, J. Zhou, L. Chen, D. P. Tsai, Metasurface enabled high-order differentiator. *Nat. Commun.* **16**, 2437 (2025).
12. Ç. Işıl, T. Gan, F. O. Ardic, K. Mentesoglu, J. Digani, H. Karaca, H. Chen, J. Li, D. Mengu, M. Jarrahi, K. Akşit, A. Ozcan, All-optical image denoising using a diffractive visual processor. *Light Sci. Appl.* **13**, 43 (2024).
13. S. K. Chamoli, C. Jin, Y. Fan, M. Kiani, H. Goh, C. Huang, S. Guo, Y. Wang, F. Zhu, G. Xing, B. Li, T. Bai, A. Alù, W. Li, Nonlocal flat optics for size-selective image processing and denoising. *Nat. Commun.* **16**, 4473 (2025).
14. X. Zhang, X. Zhang, Y. Duan, L. Zhang, X. Ni, All-optical geometric image transformations enabled by ultrathin metasurfaces. *Nat. Commun.* **14**, 8374 (2023).
15. B. Bai, X. Yang, T. Gan, J. Li, D. Mengu, M. Jarrahi, A. Ozcan, Pyramid diffractive optical networks for unidirectional image magnification and demagnification. *Light Sci. Appl.* **13**, 178 (2024).
16. N. M. Estakhri, B. Edwards, N. Engheta, Inverse-designed metastructures that solve equations. *Science* **363**, 1333–1338 (2019).
17. X. Lin, Y. Rivenson, N. T. Yardimci, M. Veli, Y. Luo, M. Jarrahi, A. Ozcan, All-optical machine learning using diffractive deep neural networks. *Science* **361**, 1004–1008 (2018).
18. P. Huo, L. Tan, Y. Jin, Y. Zhang, M. Liu, P. Lin, S. Zhang, Y. Wang, H. Ren, Y. Lu, T. Xu, Broadband and parallel multiple-order optical spatial differentiation enabled by Bessel vortex modulated metalens. *Nat. Commun.* **15**, 9045 (2024).
19. M. Cotrufo, S. Singh, A. Arora, A. Majewski, A. Alù, Polarization imaging and edge detection with image-processing metasurfaces. *Optica* **10**, 1331–1338 (2023).
20. P. Tang, Y. Kim, T. Badloe, L. Xiao, Y. Yang, M. Kim, J. Rho, G. Li, Polarization-independent edge detection based on the spin–orbit interaction of light. *Opt. Express* **32**, 17560–17570 (2024).
21. I. Tanriover, S. A. Dereshgi, K. Aydin, Metasurface enabled broadband all optical edge detection in visible frequencies. *Nat. Commun.* **14**, 6484 (2023).
22. M. Cotrufo, S. B. Sulejman, L. Wesemann, M. A. Rahman, M. Bhaskaran, A. Roberts, A. Alù, Reconfigurable image processing metasurfaces with phase-change materials. *Nat. Commun.* **15**, 4483 (2024).
23. H. Wang, M. Brady, Real-time corner detection algorithm for motion estimation. *Image Vis. Comput.* **13**, 695–703 (1995).
24. M. Trajković, M. Hedley, Fast corner detection. *Image Vis. Comput.* **16**, 75–87 (1998).
25. E. Rosten, T. Drummond, Machine learning for high-speed corner detection. *Computer Vision–ECCV 2006: 9th European Conference on Computer Vision*, Graz, Austria, May 7-13, 2006. Proceedings, Part I 9. Springer, 2006.
26. E. Rosten, R. Porter, T. Drummond, Faster and better: A machine learning approach to corner detection. *IEEE Trans. Pattern Anal. Mach. Intell.* **32**, 105–119 (2008).
27. J. Chen, L. Zou, J. Zhang, L. Dou, The comparison and application of corner detection algorithms. *J. Multimed.* **4**, 435–441 (2009).
28. K. Kohlmann, Corner detection in natural images based on the 2-D Hilbert transform. *Signal Process.* **48**, 225–234 (1996).
29. L. Huang, X. Chen, H. Mühlenbernd, G. Li, B. Bai, Q. Tan, G. Jin, T. Zentgraf, S. Zhang, Dispersionless phase discontinuities for controlling light propagation. *Nano Lett.* **12**, 5750–5755 (2012).
30. D. A. B. Miller, Attojoule optoelectronics for low-energy information processing and communications. *J. Lightwave Technol.* **35**, 346–396 (2017).
31. R. S. Williams, What's next? [the end of Moore's law]. *Comput. Sci. Eng.* **19**, 7–13 (2017).
32. P. L. McMahon, The physics of optical computing. *Nat. Rev. Phys.* **5**, 717–734 (2023).
33. C. Chen, S. Gao, W. Song, H. Li, S. Zhu, T. Li, Metasurfaces with planar chiral meta-atoms for spin light manipulation. *Nano Lett.* **21**, 1815–1821 (2021).

Acknowledgments: We acknowledge the micro-fabrication center of the National Laboratory of Solid State Microstructures (NLSSM) for technique support. **Funding:** We acknowledge the funding provided by the National Key R&D Program of China 2024YFA1012600, National Natural Science Foundation of China no. 62325504, no. 62305149, no. 62375232, and the University Grants Committee/Research Grants Council of the Hong Kong Special Administrative Region China Project No. AoE/P-502/20, CRF Project: C5031-22G and C5078-24G, GRF Project: CityU11305223, CityU11300224, CityU11304925, CityU11305125, and City University of Hong Kong Project No. 9380131. **Author contributions:** Conceptualization: C.C., D.P.T., T.L., and S.Z. Writing—original draft: C.C. Investigation: C.C., J.W., R.L., W.S., and T.L. Writing—review and editing: C.C., J.W., W.S., D.P.T., and T.L. Methodology: C.C., J.W., and T.L. Resources: C.C., J.S., D.P.T., and T.L. Funding acquisition: C.C., D.P.T., T.L., and S.Z. Data curation: C.C., J.S., and T.L. Validation: C.C., J.W., W.S., T.L., and S.Z. Formal analysis: C.C., J.W., J.S., D.P.T., and T.L. Software: C.C. and J.W., Project administration: C.C., D.P.T., T.L., and S.Z. Visualization: C.C., J.W., R.L., W.S., and T.L. Supervision: D.P.T., T.L., and S.Z. **Competing interests:** The authors declare that they have no competing interests. **Data, code, and materials availability:** All data and code needed to evaluate and reproduce the results in the paper are present in the paper and/or the Supplementary Materials. This study did not generate new materials.

Submitted 11 November 2025
Accepted 2 April 2026
Published 6 May 2026
10.1126/sciadv.aed8301

Downloaded from https://www.science.org on May 06, 2026

ScienceAdvances

Optical corner detection with azimuthal Hilbert transform metasurfaces

Chen Chen, Junyi Wang, Rong Lin, Jiacheng Sun, Wange Song, Shining Zhu, Tao Li, and Din Ping Tsai

Sci. Adv. **12** (19), eaed8301. DOI: 10.1126/sciadv.aed8301

View the article online
https://www.science.org/doi/10.1126/sciadv.aed8301
Permissions
https://www.science.org/help/reprints-and-permissions

Downloaded from https://www.science.org on May 06, 2026

Use of this article is subject to the Terms of service

Science Advances (ISSN 2375-2548) is published by the American Association for the Advancement of Science. 1200 New York Avenue NW, Washington, DC 20005. The title *Science Advances* is a registered trademark of AAAS.

Copyright © 2026 The Authors, some rights reserved; exclusive licensee American Association for the Advancement of Science. No claim to original U.S. Government Works. Distributed under a Creative Commons Attribution NonCommercial License 4.0 (CC BY-NC).